Full Length Article

A novel electrochemical kidney injury molecule-1 (KIM-1) immunosensor based covalent organic frameworks-gold nanoparticles composite and porous $NiCo_2S_4@CeO_2$ microspheres: The monitoring of acute kidney injury

Havva Boyacıoğlu [a], Bahar Bankoğlu Yola [b], Ceren Karaman [c], Onur Karaman [d], Necip Atar [a], Mehmet Lütfi Yola [e,*]

[a] Pamukkale University, Faculty of Engineering, Department of Chemical Engineering, Denizli, Turkey
[b] Iskenderun Technical University, Science and Technology Application and Research Laboratory, Hatay, Turkey
[c] Akdeniz University, Vocational School of Technical Sciences, Department of Electricity and Energy, Antalya, Turkey
[d] Akdeniz University, Vocational School of Health Services, Department of Medical Imaging Techniques, Antalya, Turkey
[e] Hasan Kalyoncu University, Faculty of Health Sciences, Department of Nutrition and Dietetics, Gaziantep, Turkey

ARTICLE INFO

ABSTRACT

Acute kidney injury is among the most severe health problems today, with the greatest fatality ratios. The kidney injury molecule-1 (KIM-1) is considered to be a potential biomarker for diagnosis of the acute kidney injury. Herein, a sensitive, selective, and swift sandwich-type electrochemical KIM-1 immunosensor was fabricated based on porous $NiCo_2S_4@CeO_2$ microspheres as a signal amplifier and covalent organic frameworks-gold nanoparticles (COFs-AuNPs) composite as an electrochemical sensor platform. The affinity of amino-gold between capture antibody and COFs-AuNPs composite led to immobilization of the capture antibody. The secondary antibody was then conjugated to $NiCo_2S_4@CeO_2$ microspheres via electrostatic interactions. Transmission electron microscopy (TEM), scanning electron microscopy (SEM), fourier-transform infrared spectroscopy (FTIR), x-ray diffraction (XRD) and x-ray photoelectron spectroscopy (XPS) techniques were performed to characterize the as-prepared materials. Some electrochemical characterization techniques including cyclic voltammetry (CV), electrochemical impedance spectroscopy (EIS) and differential pulse voltammetry (DPV) were employed to gradually characterize the constructed immunosensor. The detection limit (LOD) of KIM-1 in plasma samples was calculated as 2.00 fg mL^{-1}, making it an effective tool for the monitoring of acute kidney injury.

1. Introduction

Acute kidney injury (AKI), a prevalent severe illness with significant treatment expenses, frequently causes hospitalized patients to die [1–3]. AKI is observed in approximately 5% of hospitalized patients, 27% of patients in the critical care unit, and more than 30% of adults after heart surgery, with 3% requiring dialysis, and the fatality rate reaches more than 70% [4,5]. Despite significant technological advancements in therapy, the mortality rates linked with acute kidney injury remain high. Although serum creatinine and urine volume are routinely used to determine AKI in primary care, they are an imprecise indicator during acute alterations in renal function [6,7]. Urine volume and serum creatinine, on the other hand, are important indicators of renal function rather than kidney injury [8,9]. Hence, there is a considerable need for alternative biomarkers to detect kidney injury with high precision. The KIM-1 is considered to be the most viable protein among blood and/or urine biomarkers thanks to its applicability in the earlier diagnosis of AKI. Moreover, KIM-1 is capable of invasively expressing the injury and recovery processes [10]. Since kidney injury molecule-1 is not present in healthy people's urine, its detection can be employed as an appropriate biomarker for acute kidney injury [11–15]. Traditionally, KIM-1 tracking is performed through enzyme-linked immunosorbent assays which take approximately 3–4 h, or the microsphere-based Luminex xMAP methods, needing a massive optical analysis tool [11]. Although

---

* Corresponding author.
  E-mail address: mlutfi.yola@hku.edu.tr (M.L. Yola).

these methods' lower limits of quantification and high durability features have been verified, there is still a substantial need for developing cost-effective, easy, and convenient ways. Owing to its versatility, flexibility, swift inquiry time, low energy requirement, and cheap cost of the tool, electrochemical sensing approaches have been considered amongst the most sensitive and facile techniques for the detection of substances [16]. In particular, the electrochemical immunosensor associated with the high-affinity antibody-antigen synergy may reach superior specificity for KIM-1 biomarker monitoring [17,18]. Bioenzymes are commonly utilized as catalysts in conventional electrochemical immunosensors, however, they have some drawbacks such as poor stability and high expense [19]. As a result, over the last quarter, non-enzymatic electrochemical immunosensors have become increasingly attractive [20–22].

As a consequence of the rapid advancement of nanomaterial breakthroughs, numerous nanomaterials have been used in the fabrication of non-enzymatic electrochemical immunosensors due to their several advantages including high stability, robust electrocatalytic performance, and simplicity of modification [23,24]. Amongst the various metal-based nanostructures, gold nanoparticles (AuNPs) with a diameter range between 1 nm and 100 nm is of peculiar features such as superior electrical conductivity and stability in electrochemical sensor applications [25,26]. AuNPs can lower the overpotential of electrochemical reaction and enhance the redox reaction reversibility. Furthermore, by tuning the AuNPs, the oxidation reaction between the surface of sensor and the electroactive molecules may be accelerated [27].

Organic monomers linkers have been used to prepare porous and crystalline COFs via reversible covalent bonding [28–31]. Currently, COFs have been utilized in several applications such as gas storage [32], catalysis [31] and photoelectrochemistry [33]. COFs have a number of benefits including uniform pore distribution, unique electronic system, and thermal stability [34]. In addition, it provides superior scaffolds for charge migration and the signal amplification improvement [35]. Generally, due to polymers' wide pore size, the polymeric structures cause irregular channels, providing an average path for proton transport. COFs, on the other hand, as a crystalline substance, have a distinct pore size distribution that allows protons to easily diffuse [35]. As a result of COFs' large specific surface area and tunable pore structure, effective and functional sensors/biosensors can be fabricated.

$NiCo_2S_4$ as the electrode material has gained significant attention owing to its high theoretical specific capacitance, superior cycling stability, and low cost [36,37]. However, the poor conductivity of transition metal sulfides significantly hampers the reversible capacitance and cycling stability [38,39]. Several methods have been proposed to overcome these problems, the preparation of the $NiCo_2S_4$ based nanostructures including carbonaceous materials [40] or transition metal oxides [41] are also amongst these methods. Cerium dioxide (CeO_2) is of rich oxygen vacancies, thereby providing the easy conversion between Ce^{3+} and Ce^{4+}, and facilitating the charge transfer from CeO_2 to the sensor surface [42]. Therefore, it is presumed that the preparation of $NiCo_2S_4@CeO_2$ composite is one of the effective ways for enhancing of the electrochemical performance. Furthermore, the three-dimensional microspheres with mesoporous pore structure can offer high mechanical strength, superior electrical conductivity, and efficient specific surface area facilitating the permeation of the electrolyte at the electrochemical sensor platform surface. The reshaping of morphology via the incorporation of the active materials is regarding an effective way for enhancing the specific surface area, reversible capacitance, and stability [43].

Herein, in the light of all aforementioned points in mind, the main objective of this paper was to construct an innovative electrochemical KIM-1 immunosensor based on porous $NiCo_2S_4@CeO_2$ microspheres and COFs-AuNPs for the first time in the literature. The fabricated immunosensor provided a number of benefits, including simplicity, fast response time, and selectivity. A precise LOD of 2.00 fg mL^{-1} was determined with superior selectivity and no interference in plasma samples. Hence, it can be speculated that the fabricated electrochemical KIM-1 immunosensor may open a new perspective in the facile and swift monitoring of acute kidney injury.

2. Experimental

2.1. Materials

Kidney injury molecule-1 (KIM-1), anti-KIM-1 capture antibody (anti-KIM-1-Ab$_1$), anti-KIM-1 secondary antibody (anti-KIM-1-Ab$_2$), bovine serum albumin (BSA), α-fetoprotein (AFP), cystatin C (CysC), prostate-specific antigens (PSA), $NiCl_2 \cdot 6H_2O$, $CoCl_2 \cdot 6H_2O$, cetyltrimethyl ammonium bromide (CTAB), $Na_2S \cdot 9H_2O$, sodium dodecyl sulfate (SDS), $Ce(NO_3)_3 \cdot 6H_2O$, 3,5-tris(4-aminophenyl)benzene (TAB), p-phthalaldehyde (PTA), dimethyl sulfoxide (DMSO), trisodium citrate (TSC) and gold(III) chloride hydrate ($HAuCl_4$) were supplied from Sigma-Aldrich. As a supporting electrolyte and diluting buffer solution, a 0.1 M phosphate-buffered saline (PBS) solution (pH = 7.0) was utilized.

2.2. Apparatus for evaluation of nanomaterials

Surface morphological characteristics were explored by using a ZEISS EVO 50 SEM and a JEOL 2100 TEM. X-ray patterns of nanomaterials was collected by a Rigaku X-ray diffractometer with Cu-K radiation (λ = 0.150 nm). The PHI 5000 Versa Probe spectrometer was used to perform the XPS survey. UV–Vis and FTIR measurements were performed by Mettler Toledo and Bruker-Tensor FTIR spectrometer, respectively. Electrochemical characterization techniques such as CV, EIS and DPV were also conducted via the Gamry Reference 600 workstation (Gamry, USA).

2.3. Preparation of COFs based on TAB and PTA

The dispersion of TAB (0.100 g) and PTA (0.05 g) was prepared in DMSO (100.0 mL) under vigorous stirring over 10 min. Following, CH_3COOH (2.0 mL) was introduced to the resulting solution and incubated at 25 °C for 45 min. Followed by the centrifugation at 5000 rpm, **COFs** based on TAB and PTA was collected and rinsed two times with ethanol. After the drying at 60 °C, COFs was grounded into powder [44].

2.4. Preparation of COFs-AuNPs composite and GCE modification with COFs-AuNPs as electrochemical sensor platform (COFs-AuNPs/GCE)

Followed by the ultrasonication of COFs (30.0 mg) in deionized (DI) water, TSC (30.0 mmol, 4.0 mL) was gently poured into as-obtained solution under magnetic stirring. After the boiling treatment, $HAuCl_4$ solution (2.0%, 750.0 μL) was promptly added under stirring for 20 min, providing brown conversion. Subsequently, the **COFs-AuNPs** composite was washed with ethanol two times, followed by drying treatment under a vacuum medium.

The glassy carbon electrode (GCE) was prepared as follows to be utilized in the further steps [45]: Firstly, 0.1 μm and 0.05 μm alumina (Al_2O_3) slurries were transferred on cleaning pads, respectively. Following, the GCE was polished with these Al_2O_3 slurries for 20 min. Subsequently, the electrodes were rinsed with isopropyl alcohol and acetonitrile, respectively to eliminate the residual alumina, and dried at 25 °C. The electrode modifications with COFs and COFs-AuNPs composite dispersions (15.0 μL, 0.2 mg mL^{-1}) were performed by a simple drop-casting method inclusing coating the related dispersions onto the clean GCEs surface dropwisely. After 20 min, the solvent evaporation from the electrode surface was accomplished by an infrared (IR) heat lamp, thereby resulting COFs and COFs-AuNPs modified GCEs (**COFs/GCE** and **COFs-AuNPs/GCE**).
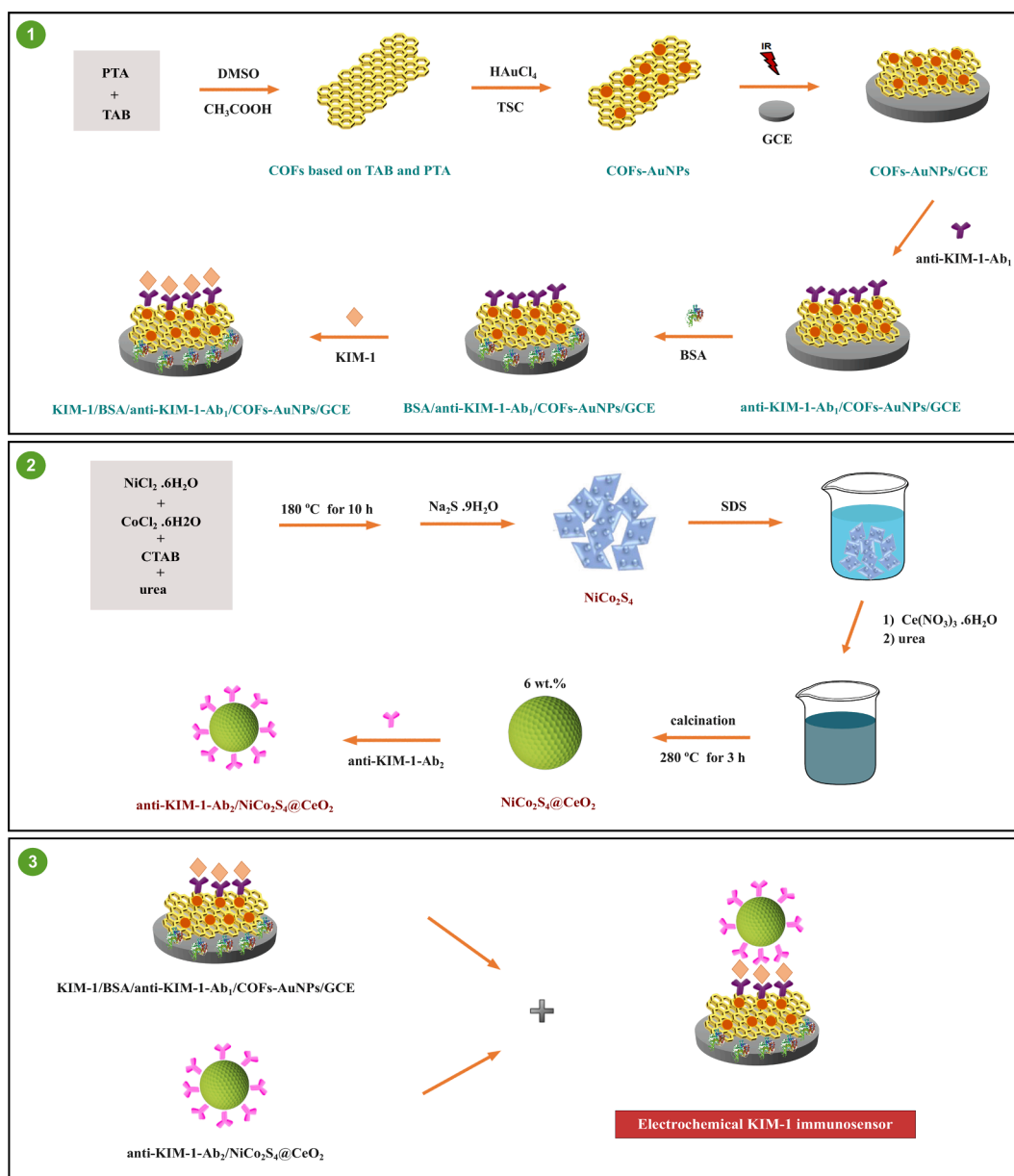
Scheme 1. Schematic illustration of the fabrication procedure of electrochemical KIM-1 immunosensor.

2.5. anti-KIM-1-Ab₁ and antigen KIM-1 immobilizations on COFs/GCE and COFs-AuNPs/GCE

The anti-KIM-1-Ab$_1$ immobilization on COFs-AuNPs/GCE was conducted by introducing anti-KIM-1-Ab$_1$ dispersion (20.0 μL, 20.0 μg mL^{-1}) onto the COFs-AuNPs/GCE via strong amino-gold interactions. The prepared electrode was kept at 37.0 °C over 15 min (***anti-KIM-1-Ab₁/COFs-AuNPs/GCE***). Afterward, BSA (3.0% w/v) was incubated on anti-KIM-1-Ab$_1$/COFs-AuNPs/GCE at 37.0 °C over 15 min to eliminate the non-specific interactions (***BSA/anti-KIM-1-Ab₁/COFs-AuNPs/GCE***). The KIM-1 solutions at each specified concentration values interacted with BSA/anti-KIM-1-Ab1/COFs-AuNPs/GCE through specific antigen–antibody interactions over 15 min at 37.0 °C (***KIM-1/BSA/anti-KIM-1-Ab₁/COFs-AuNPs/GCE***). At the end, the final electrode containing KIM-1 and anti-KIM-1-Ab1 was treated with 0.1 M PBS (pH 7.0) to eliminate non-interacted antigens and antibodies.

2.6. Preparation of NiCo₂S₄ and NiCo₂S₄@CeO₂ microspheres

The mixture of NiCl$_2$·6H$_2$O (8.0 mmol) and CoCl$_2$·6H$_2$O (16.0 mmol) was firstly prepared in ethanol and deionized water (1:1, v/v). Subsequently, CTAB (2.0 g) and urea (25.0 mmol) were added into the as-obtained mixture under the vigorous stirring for 45 min. The resultant dispersion was placed into Teflon stainless autoclave and subjected to the heating treatment at 180 °C for 10 h. Following cooling to 25 °C, centrifugation at 10000 rpm was conducted, and the resulting product was washed twice with ethanol. After the preparation of Na$_2$S·9H$_2$O solution (30.0 mmol/L) in DI water, the solution was slowly added into Ni-Co precursor. Afterward, the resultant mixture was heated at 150 °C for 12 h and washed with ethanol two times, providing ***NiCo₂S₄*** microspheres.

The NiCo$_2$S$_4$ microspheres (0.50 g) and SDS (0.25 g) was dispersed in a solution of ethanol and deionized water (1:1, v/v) (Solution 1). Ce (NO$_3$)$_3$·6H$_2$O solution (Solution 2) and the urea (0.20 g) solution were prepared in deionized water and labeled as Solution 2 and Solution 3, respectively. Subsequently, Solution 2 and Solution 3 were slowly added
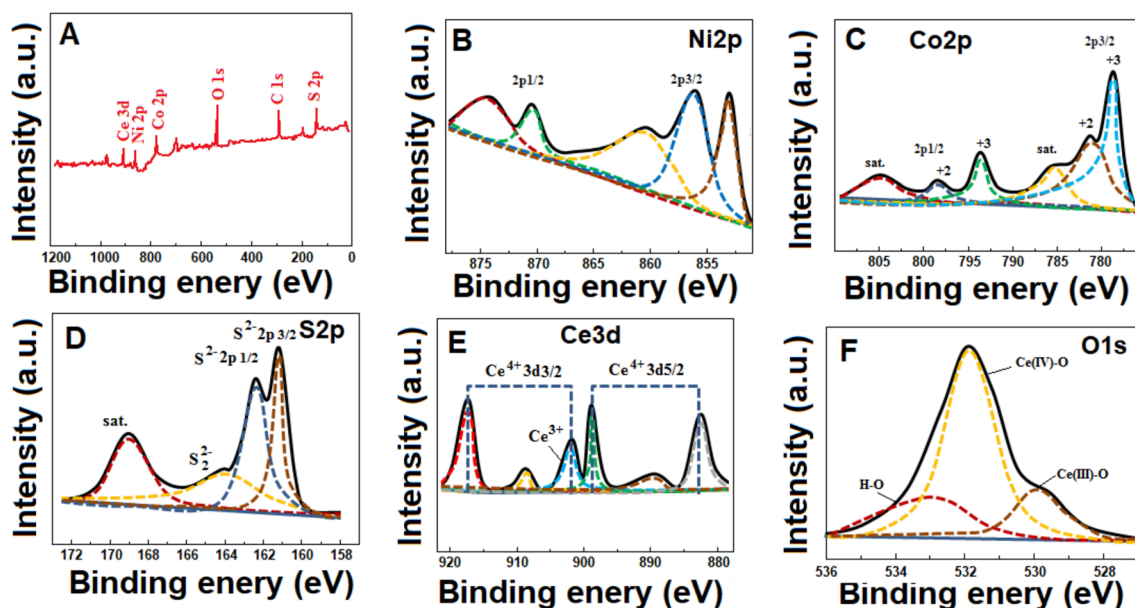
Fig. 1. (A) XPS spectra for $NiCo_2S_4@CeO_2$ microspheres, high-resolution of (B) Ni2p, (C) Co2p, (D) S2p, (E) Ce3d and (F) O1s of $NiCo_2S_4@CeO_2$ microspheres.

into Solution 1 for 4 h. The as-obtained solution was transferred into Teflon stainless autoclave reactor and heated at 150 °C for 12 h. After that, the product was calcined at 280 °C for 3 h under a high purity argon atmosphere to acquire ***NiCo₂S₄@CeO₂*** (6.0 wt%) microsphere powders [46].

2.7. $NiCo_2S_4@CeO_2$ microspheres signal amplification with anti-KIM-1-Ab_2 conjugation

anti-KIM-1-Ab_2 conjugation was performed by addition of secondary antibody (20.0 μL, 20.0 μg mL^{-1}) into $NiCo_2S_4@CeO_2$ (20.0 μL, 20.0 mg mL^{-1}) signal amplification via strong electrostatic interactions. After the vigorous stirring at 37.0 °C for 30 min, ***anti-KIM-1-Ab₂/NiCo₂S₄@CeO₂*** was centrifugated at 5000 rpm for 30 min.

2.8. Electrochemical evaluations

The resulting KIM-1 immunosensor was constructed by antibody-antigen interactions between anti-KIM-1-Ab_2/$NiCo_2S_4@CeO_2$ and KIM-1/BSA/anti-KIM-1-Ab_1/COFs-AuNPs/GCE. anti-KIM-1-Ab_2/$NiCo_2S_4@CeO_2$ dispersion (20.0 μL, 20.0 mg mL^{-1}) was dropped on electrode surface at a 30 min immunological response time. The final electrochemical immunosensor was tagged as ***NiCo₂S₄@CeO₂/anti-KIM-1-Ab₂/KIM-1/BSA/anti-KIM-1-Ab₁/COFs-AuNPs/GCE***, and it was stored in 0.1 M PBS (pH 7.0, 3.0 mL) without pressure fluctuations at 25 °C. The electrochemical performance of KIM-1 immunosensor was monitored in 0.1 M PBS (pH 7.0, 2.0 mL) containing 1.0 mM H_2O_2 solution in the potential range of + 0.0/+0.4 V.

2.9. Processing of samples

Sample preparation process was detailed on Supplementary Data [47].

3. Results and discussion

3.1. Fundamental of electrochemical KIM-1 immunosensor based on COFs-AuNPs as electrochemical sensor platform and $NiCo_2S_4@CeO_2$ microspheres as signal amplification

Fundamentals of electrochemical KIM-1 immunosensor were

illustrated on Scheme 1. TAB and PTA as monomer materials were used for the preparation of covalent organic frameworks by ultrasonic solvent method through imine bonding. COFs based on TAB and PTA provided large electrochemical sites for the incorporation of AuNPs and increased the specific surface area of the electrode. The combination of COFs based on TAB and PTA with AuNPs peformed the binding between Au and amino groups. After the modification of GCE with COFs-AuNPs composite by IR lamp, both of surface area and electrochemical conductivity improved, thereby providing more KIM-1 immobilizations on electrochemical sensor platform via the high affinity between amino groups of KIM-1 and gold elements of COFs-AuNPs composite.

$NiCo_2S_4$ microspheres having nanoparticles were prepared by a hydrothermal process. Afterward, $NiCo_2S_4@CeO_2$ microspheres with nanosheets were tailored by a morphology reshaping process. The incorporation of CeO_2 altered the nanoparticle morphology of $NiCo_2S_4$, thereby rendering incompact nanosheet. The porous and incompact nanosheet areas not only increased the charge transfer but also facilitated the electrochemical diffusion, leading more electrochemically active sites for antibody conjugation. In immunosensor construction, the strong physical electrostatic interactions between amino group of anti-KIM-1-Ab_2 and porous $NiCo_2S_4@CeO_2$ microspheres also provided the seconder antibody immobilization on electrode surface. Finally, H_2O_2 was utilized as a redox probe in this work due to its easy oxidation into O_2 and continuous monitoring [22,24].

3.2. Characterizations of $NiCo_2S_4$ and $NiCo_2S_4@CeO_2$ microspheres

Fig. S1 demonstrated XRD patterns of $NiCo_2S_4$ and $NiCo_2S_4@CeO_2$ (6.0 wt%) microspheres. The XRD peaks detected at 16.43°, 27.11°, 32.07°, 50.63° and 55.43° were attributed to (111), (220), (311), (400), (511) and (400) planes corresponding $NiCo_2S_4$ [48]. The novel XRD peaks observed at 28.32°, 47.69° and 56.27° were attributed to the (111), (220) and (311) planes of CeO_2 [49]. There were no other XRD peaks observed, confirming the preparation of high purity $NiCo_2S_4$ and $NiCo_2S_4@CeO_2$ microspheres. XPS analysis was carried out to enlighten the chemical states of $NiCo_2S_4@CeO_2$ microspheres (Fig. 1). According to Fig. 1A of the full range XPS survey spactra, the peaks belonging to Ni, Co, S, Ce and O elements confirmed the succesful preparation of $NiCo_2S_4@CeO_2$ microspheres. Ni2p XPS spectrum (Fig. 1B) deconvoluted into Ni2p3/2 and Ni2p1/2 offered the coexistence of Ni^{2+} and Ni^{3+} for $NiCo_2S_4$ [50]. According to Fig. 1C, two spin–orbit doublets at 786.1 and
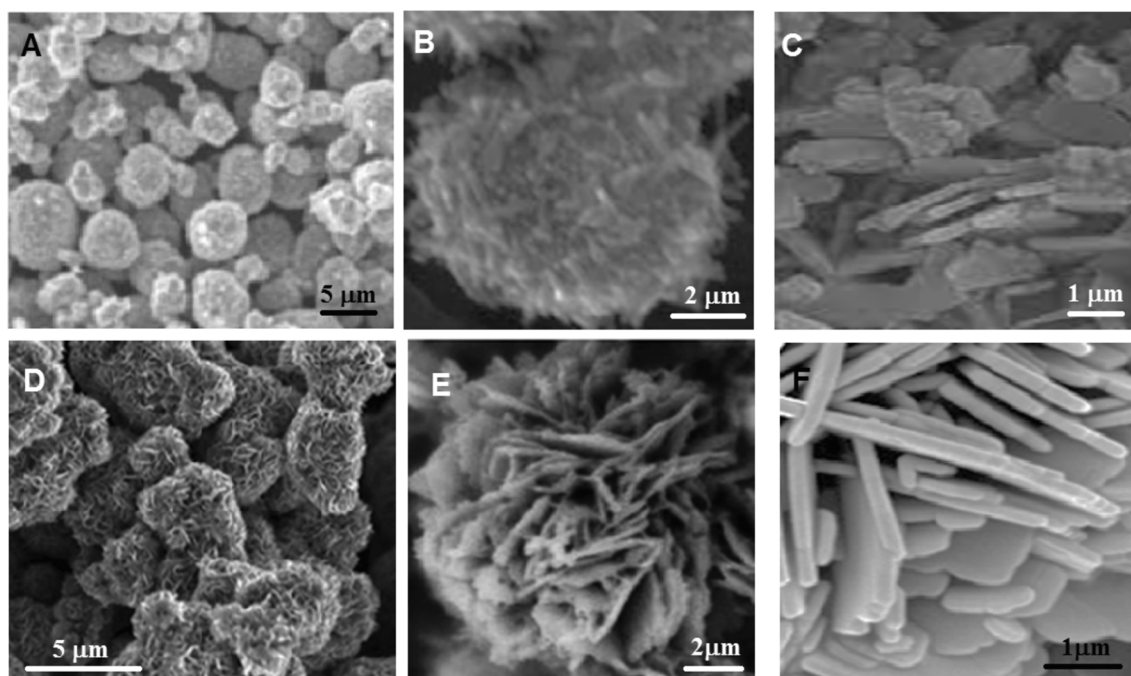
Fig. 2. SEM images of (A-C) pristine $NiCo_2S_4$ and (D-F) $NiCo_2S_4@CeO_2$ (6.0 wt%) microspheres.

803.1 eV were corresponded to satellites peaks. In addition, the peaks at 794.1 and 779.1 eV were attributed to Co^{3+}, whereas the peaks at 781.1 and 798.2 eV were ascribed to Co^{2+} [51]. Moreover, the peaks (Fig. 1D) at 161.68 and 163.03 eV were corresponded to S2p1/2 and S2p3/2, respectively, confirming the presence of S^{2-} ion at a low coordination state. In addition, the peak at 163.44 eV was attributed to M−S (M = Co and Ni) bonds [52]. For Ce3d spectrum (Fig. 1E), the peaks at 882.15, 889.07 and 899.96 eV were corresponded to Ce3d5/2 whereas the peaks at 901.64, 903.16, 908.18 and 917.16 eV were attributed to Ce3d3/2, respectively [53]. According to XPS data, the formation of oxygen vacancy or oxygen defect occurred on $NiCo_2S_4@CeO_2$ microspheres, indicating the boosted electronic conductivity [46]. The peaks at 530.11 and 531.78 eV corresponding to Ce-O and oxygen vacancy, respectively and the peak at 533.07 eV attributing to the chemisorbed oxygen were observed in O1s spectra (Fig. 1F) [46].

SEM characterizations (Fig. 2) were performed to examine the morphological features of $NiCo_2S_4$ and $NiCo_2S_4@CeO_2$ microspheres. The microsphere morphology having a diameter of 2–3 μm suggested pristine $NiCo_2S_4$, indicating irregular particles (Fig. 2A-C). The microsphere morphologies of pristine $NiCo_2S_4$, on the other hand, did not alter after the preparation of $NiCo_2S_4@CeO_2$ (6.0 wt%) microspheres. The porous polyhedron crystals formed after the incorporation of CeO_2 (Fig. 2D-F). In addition, an incompact nanosheets structure was formed on $NiCo_2S_4@CeO_2$ microspheres (6.0 wt%). Thus, the specific surface area enhanced thanks to the porous and incompact nanosheet structure. The interconnected nanosheets also revealed a hierarchical nano-architecture, with open space between thin blocks. Hence, $NiCo_2S_4@CeO_2$ microspheres resulted in high accessible electrochemical active surface, thereby facilitating of electron transfer. Finally, EDS mapping (Fig. S2) of $NiCo_2S_4@CeO_2$ (6.0 wt%) microspheres was acquired to verify the presence of Ni, Co, S, Ce and O, confirming a uniform distribution of CeO_2 on $NiCo_2S_4$ surface.

TEM and HR-TEM images (Fig. S3) of $NiCo_2S_4$ and $NiCo_2S_4@CeO_2$ (6.0 wt%) microspheres were also obtained for further morphological investigation. According to TEM images of $NiCo_2S_4$ (Fig. S3A) and $NiCo_2S_4@CeO_2$ (6.0 wt%) microspheres (Fig. S3C), the morphological structures of $NiCo_2S_4$ having irregular nanoparticles and $NiCo_2S_4@CeO_2$ having nanosheet were observed. In addition, according to HR-TEM

images of $NiCo_2S_4$ (Fig. S3B) and $NiCo_2S_4@CeO_2$ (6.0 wt%) microspheres (Fig. S3D), four specific interlayer spacings were calculated as 0.194, 0.269, 0.237 and 0.334 nm attributing to (4 2 2), (2 2 2), (4 0 0) and (2 2 0) planes of $NiCo_2S_4$, respectively. The interlayer spacing of 0.310 nm was also attributed to (1 1 1) plane of CeO_2. Hence, it was concluded that the successful synthesis of pristine $NiCo_2S_4$ and $NiCo_2S_4@CeO_2$ (6.0 wt%) microspheres was accomplished in harmony with XRD results.

The specific surface area and pore size distribution of $NiCo_2S_4$ and $NiCo_2S_4@CeO_2$ (6.0 wt%) microspheres were provided by nitrogen adsorption–desorption isotherm (Fig. S4) indicating type IV behavior [54,55]. The relative pressure (P/P_0) between 0.4 and 1.0 confirmed the presence of mesopores [56]. The specific surface area of $NiCo_2S_4$ and $NiCo_2S_4@CeO_2$ (6.0 wt%) microspheres were obtained as 39.873 $m^2\,g^{-1}$ and 137.073 $m^2\,g^{-1}$, respectively. As a result, it was concluded that the incorporation of CeO_2 increased morphology reshaping, thereby facilitating the electrolyte permeation and electron transfer rate [46].

3.3. Characterizations of COFs-AuNPs

TEM micrograph (Fig. 3) was obtained for morphological investigations of COFs based on TAB and PTA and COFs-AuNPs composite. COFs based on TAB and PTA including thin sheet structures (Fig. 3A) and the incorporation of AuNPs into COFs based on TAB and PTA (Fig. 3B) were observed. According to EDS mapping (Fig. 3C), the presence of C, N, O and Au elements confirmed the successful synthesis of COFs-AuNPs composite. In addition, C elements formed the basic skeleton and the other three elements (C, O and N) were dispersed homogeneously. However, the less uniform distribution of AuNPs was observed in comparison with the other elements. This condition can arise as a result of the accumulation of sheet-like COFs based on TAB and PTA, obstructing the distribution of AuNPs. Moreover, XRD patterns (Fig. S5A) of COFs based on TAB and PTA and COFs-AuNPs composite were recorded. According to XRD pattern of COFs based on TAB and PTA, no important XRD peaks in range of 2θ = 30°- 80° were observed. On the other hand, the XRD pattern of COFs-AuNPs composite offered the peaks at 37.93°, 44.61° and 65.09° corresponding to Au 111, 200 and 220 planes. UV–Vis spectra (Fig. S5B) of COFs based on TAB and
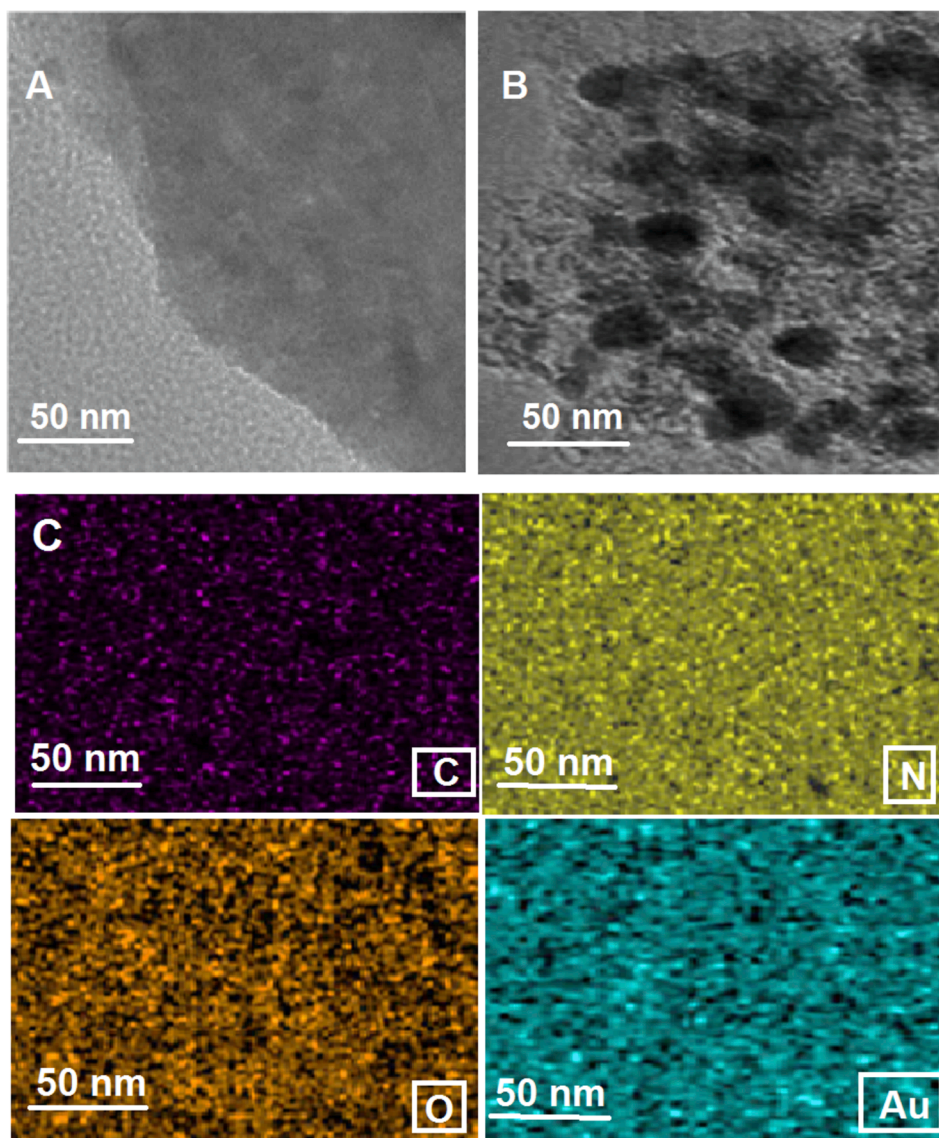
Fig. 3. TEM images of (A) COFs based on TAB and PTA, (B) COFs-AuNPs composite and (C) the corresponding element distribution mapping of C, N, O and Au of COFs-AuNPs composite.

PTA and COFs-AuNPs composite were obtained. The absorption band at 530 nm corresponding to AuNPs and the absorption band at 461 nm attributing to COFs based on TAB and PTA were observed in harmony with the literature [26]. The red-shift on the absorption band of AuNPs from 530 nm to 555 nm confirmed the partial incorporation of AuNPs on the composites.

Fig. S6 demonstrated the FTIR spectra of TAB, PTA, COFs based on TAB and PTA and COFs-AuNPs composite. The specific peaks at 3430, 3351 and 3211 cm^{-1} on FTIR spectrum of TAB were attributed to the stretching vibration resulting from —NH group. The absorption band at 1697 cm^{-1} on FTIR spectrum of PTA indicated the presence of —C═O absorption. In addition, the absorption peaks at 1510 cm^{-1} were corresponded to —C—C— stretching vibration [57]. The specific peak at 1620 cm^{-1} indicated —C═N of COFs based on TAB and PTA. Moreover, the disappearances of —C═O— vibration and TAB amino group's reduction revealed that the complex formation between TAB and PTA resulted from the condensation reaction of amino and carboxyl groups. —C—C— stretching vibration on COFs based on TAB and PTA and COFs-AuNPs composite decreased in comparison with the peak at 1510 cm^{-1}. The decrease in the peak intensity suggested that TAB's benzene ring and PTA's —C═O— group formed an imino bond. FTIR spectra of COFs

based on TAB and PTA and COFs-AuNPs composite were essentially identical, indicating that incorporation of AuNPs had little influence on the structural characteristics of COFs based on TAB and PTA. Finally, the absorption bands observed at *ca.*3341 cm^{-1} confirmed the presence of carboxyl groups. These absorption bands resulted from the acid remained in the complex after the preparation of COFs based on TAB and PTA.

XPS analysis was carried out to examine the chemical states of COFs based on TAB and PTA and COFs-AuNPs composite (Fig. S7). According to Fig. S7A of the full range XPS survey spactra, the peaks belonging to C, N, O and Au elements confirmed the succesful preparation of the composite. Au4f XPS spactra (Fig. S7B) demonstrated the complete reduction of Au(0) in presence of excess TSC. In addition, N1s spectrum (Fig. S7C) proved the presence of –NH$_2$ groups on COFs based on TAB and PTA at 400.04 eV. Nonetheless, the binging energy of N1s on COFs-AuNPs composite was higher in comparison with COFs based on TAB and PTA. This decrease was caused by the interaction between –NH$_2$ group and Au [44,58].

The specific surface area and pore size distribution of COFs based on TAB and PTA and COFs-AuNPs composite were provided by nitrogen adsorption–desorption isotherm (Fig. S8A). The pore volume and
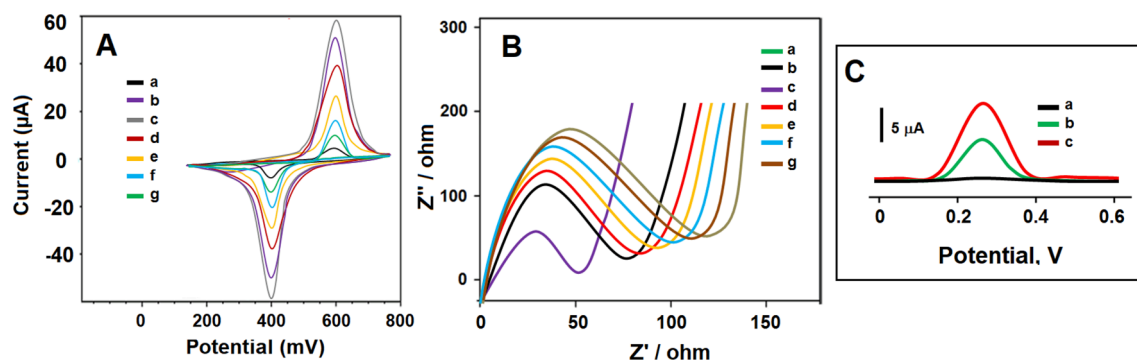
Fig. 4. (A) Cyclic voltammograms, (B) EIS reponses at (a) bare GCE, (b) COFs/GCE, (c) COFs-AuNPs/GCE, (d) anti-KIM-1-Ab$_1$/COFs-AuNPs/GCE, (e) BSA/anti-KIM-1-Ab$_1$/COFs-AuNPs/GCE, (f) KIM-1/BSA/anti-KIM-1-Ab$_1$/COFs-AuNPs/GCE, (g) the final immunosensor including anti-KIM-1-Ab$_1$, KIM-1 and anti-KIM-1-Ab$_2$ (scan rate of 50 mV s^{-1}) in 1.0 mM [Fe(CN)$_6$]$^{3-}$ containing 0.1 M KCl and (C) DPV responses of the proposed immunosensors incubated with 5.00 pg mL^{-1} KIM-1 using anti-KIM-1-Ab$_2$/NiCo$_2$S$_4$ (curve b) and anti-KIM-1-Ab$_2$/NiCo$_2$S$_4$@CeO$_2$ (curve c) in absence of H$_2$O$_2$ (curve a) and in presence of 1.0 mM H$_2$O$_2$.

specific surface area were calculated as 0.173 cm^3 g^{-1} and 58.93 m^2 g^{-1} for COFs based on TAB and PTA, respectively, and the pore size and specific surface area were computed as 0.227 cm^3 g^{-1} and 65.31 m^2 g^{-1} for COFs-AuNPs composite, respectively. Thus, a larger surface area and pore volume provided more antigen KIM-1 immobilizations on electrochemical sensor platform. Lastly, the thermal stability of COFs based on TAB and PTA and COFs-AuNPs composite was also investigated (Fig. S8B). COFs based on TAB and PTA and COFs-AuNPs composite demonstrated an important mass loss after 400 °C, providing high thermal stability.

3.4. Electrochemical characterizations of sensor platform and signal amplification

The electrochemical investigations for the prepared sensor platform were progressively performed by using CV and EIS methods in the presence of 1.0 mM [Fe(CN)$_6$]$^{3-/4-}$ as redox pair. Firstly, the anodic and cathodic signals on bare GCE were observed at E$_{pa}$ = 600 mV and E$_{pc}$ = 400 mV, respectively, (curve a of Fig. 4A). When COFs/GCE was used towards 1.0 mM [Fe(CN)$_6$]$^{3-/4-}$, the more obvious electrochemical signals were obtained in comparison with bare GCE (curve b of Fig. 4A) due to the large specific surface area of COFs and tunable pore structure of it [59]. The highest electrochemical responses were observed on COFs-AuNPs/GCE (curve c of Fig. 4A) in comparison to COFs/GCE due to the enhanced catalytic activity and electrochemical conductivity of COFs-AuNPs composite [44]. However, as expected, the obvious electrochemical sensor signals decreased owing to anti-KIM-1-Ab$_1$'s blocking effect on electron transfer (curve d of Fig. 4A). After the immobilizations of BSA (curve e of Fig. 4A) and KIM-1 (curve f of Fig. 4A), respectively, it was observed that the sensor signals gradually decreased. Thus, it was concluded that the immobilization treatments of BSA and KIM-1 on electrode surface were successfully carried out. Finally, when the resulting immunosensor was used (curve g of Fig. 4A), further decrease on sensor signals were observed because of more antibody-antigen interactions.

Secondly, EIS experiments were performed to confirm the CV findings, and according to Fig. 4B, the obtained charge transfer resistances were calculated as 150, 100, 60, 110, 120, 130 and 140 ohm for bare GCE (curve a), COFs/GCE (curve b), COFs-AuNPs/GCE (curve c), anti-KIM-1-Ab$_1$/COFs-AuNPs/GCE (curve d), BSA/anti-KIM-1-Ab$_1$/COFs-AuNPs/GCE (curve e), KIM-1/BSA/anti-KIM-1-Ab$_1$/COFs-AuNPs/GCE (curve f), and the final immunosensor (curve g), respectively. Hence, it was confirmed that the preparation procedure of immunosensor was completed successfully based on CV and EIS results.

For electrochemical performance characterization (Fig. 4C) of the prepared signal amplification, several immunosensors using anti-KIM-1-Ab$_2$/NiCo$_2$S$_4$ (curve b) and anti-KIM-1-Ab$_2$/NiCo$_2$S$_4$@CeO$_2$ (curve c)
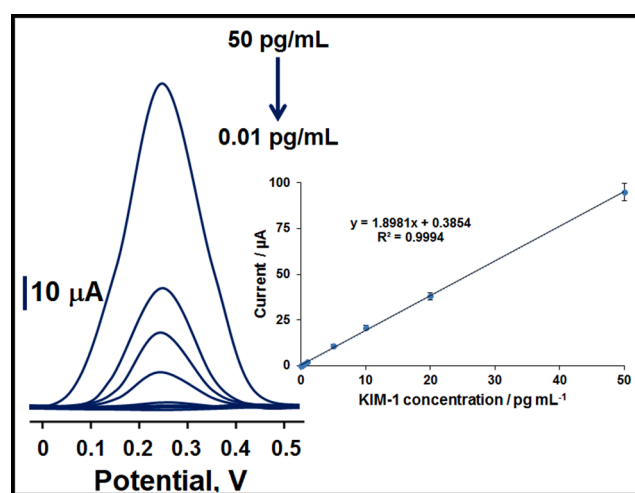

Fig. 5. Concentration effect (from 0.01 to 50.0 pg mL^{-1} KIM-1) on immunosensor signals, Inset: Calibration curve for electrochemical KIM-1 immunosensor (Potential range is + 0.0/+0.4 V; Parameters are frequency of 100 Hz, pulse amplitude of 20 mV and scan increment of 5 mV).

were developed by using 5.00 pg mL^{-1} KIM-1 at the immune reaction time of 30 min, and the DPV signals were observed in 1.0 mM H$_2$O$_2$. As expected, the highest electrochemical performance was acquired by the immunosensor based on anti-KIM-1-Ab$_2$/NiCo$_2$S$_4$@CeO$_2$ in comparison with anti-KIM-1-Ab$_2$/NiCo$_2$S$_4$ due to the incorporation of CeO$_2$ facilitating the electrolyte permeation and the electron transfer rate.

Table 1
The observed electrochemical signals for the calibration equation (n = 6).

KIM-1 concentration (pg mL^{-1})	Current signals (µA)*
0.01	0.020 ± 0.001
0.05	0.100 ± 0.002
0.1	0.200 ± 0.002
0.2	0.400 ± 0.003
0.5	1.00 ± 0.01
1.0	2.00 ± 0.03
5.0	11.00 ± 0.02
10.0	21.00 ± 0.01
20.0	38.00 ± 0.02
50.0	95.00 ± 0.03

* $\overline{X}$: Mean ± Standard Error.

Table 2
The comparison of the prepared electrochemical immunosensor with the other techniques for protein detection.

Material/Method	Target	Linear Range	LOD	Stability	Ref.
Hydroxyapatite	KIM-1	10.0–100.0 ng mL^{-1}	17.0 ng mL^{-1}	–	[11]
PdPtBP NPs/ MXene	KIM-1	0.50–100.0 ng mL^{-1}	86.0 pg mL^{-1}	93.06% (10 days)	[60]
PbS Quantum Dot	HER2	1.00–100.0 ng mL^{-1}	280.0 pg mL^{-1}	–	[61]
HRP	IgA	0. 0–250.0 ng mL^{-1}	19.0 ng mL^{-1}	90.00% (1 week)	[62]
Pt/Ru/C Nanoparticle	CRP	0.20–20.0 ng mL^{-1}	100.0 pg mL^{-1}	90.00% (1 month)	[63]
ELISA	KIM-1	0.0–5.0 pg mL^{-1}	39.0 pg mL^{-1}	5 days	[61]
Electrochemical immunosensor	*KIM-1*	*0.01–50.00 pg mL^{-1}*	*2.00 fg mL^{-1}*	*97.81% (7 weeks)*	*This study*

3.5. Optimization for electrochemical measurements

The effects of the solution pH, immune reaction time, H$_2$O$_2$, anti-KIM-1-Ab$_2$/NiCo$_2$S$_4$@CeO$_2$ solution concentration, secondary antibody (anti-KIM-1-Ab$_2$) concentration and incubation time of anti-KIM-1-Ab$_2$ were presented in detail (Fig. S9).

3.6. Linearity range

The calibration equation obtained by using both KIM-1 concentrations and the observed electrochemical immunosensor signals was calculated as $y = 1.8981x + 0.3854$, with a correlation coefficient of R^2 = 0.9994, where y and x represented the current (µA) and KIM-1 concentration (pg mL^{-1}), respectively (Fig. 5). The observed

electrochemical signals against KIM-1 concentrations were obtained by using the constructed sandwich-type electrochemical KIM-1 immunosensor on Table 1. According to Table 1, the constructed sandwich-type electrochemical KIM-1 immunosensor was used for KIM-1 detection at +0.25 V. The quantification limit (LOQ) and LOD were found to be 0.01 pg mL^{-1} and 2.00 fg mL^{-1}, respectively. Eqs. (1) and (2) were employed to calculate LOQ and LOD:

$$LOQ = 10.0S / m \tag{1}$$

$$LOD = 3.3S / m \tag{2}$$

In addition, Table 2 gave some comparison features between the constructed sandwich-type electrochemical KIM-1 immunosensor and the other protein detection methods. In this study, a novel and sensitive electrochemical KIM-1 immunosensor was firstly prepared based on porous NiCo$_2$S$_4$@CeO$_2$ microspheres as signal amplification and COFs-AuNPs composite as electrochemical sensor platform, providing early detection of acute kidney injury. The constructed immunosensor possessed satisfactory long-term stability. Especially, the elimination of the time-consuming steps in KIM-1 immunosensor preparation allowed portable usability in comparison with the other detection methods [11,60]. In addition, the production of fast DPV immunosensor signals resulted in efficient analysis in short time of 20 s. Finally, the immunosensor preparation with the minimal waste formation demonstrated that the fabricated immunosensor was friendly to the environment and human health. Hence, it can be concluded that the developed stable and reproducible electrochemical KIM-1 immunosensor may offer a potential for early disease detection.

3.7. Recovery

The recovery experiments including plasma samples were carried out by the portable electrochemical KIM-1 immunosensor. Close values to 100.00 % were reported in Table S1, supporting the fabrication of a highly selective electrochemical KIM-1 immunosensor. Moreover, the
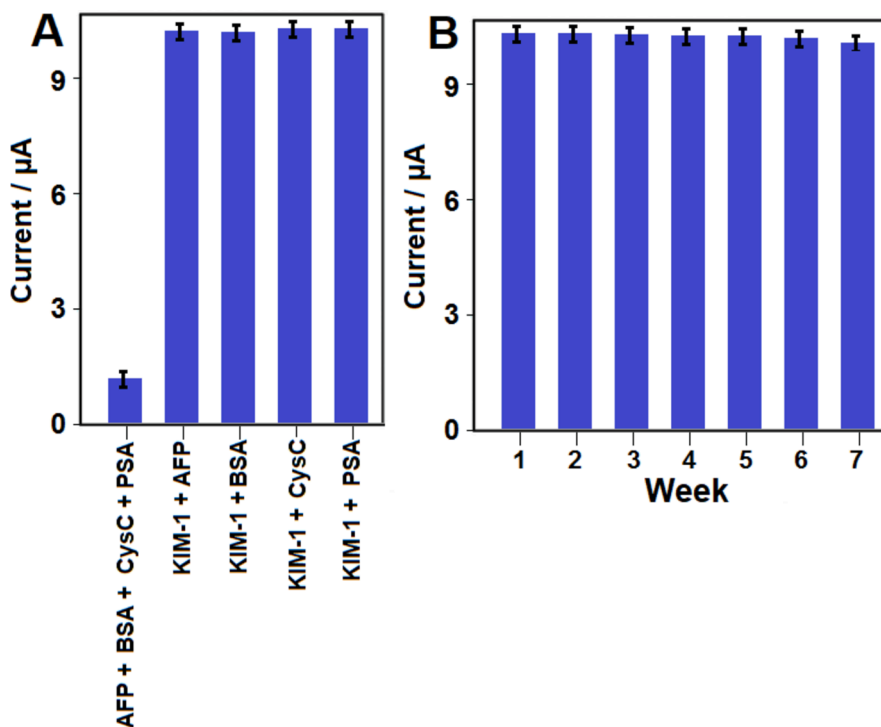

Fig. 6. (A) Immunosensor selective responses against the prepared solutions (n = 6): (i) 100.00 pg mL^{-1} AFP + 100.00 pg mL^{-1} BSA + 100.00 pg mL^{-1} CysC + 100.00 pg mL^{-1} PSA, (ii) 5.00 pg mL^{-1} KIM-1 + 100.0 pg mL^{-1} AFP, (iii) 5.00 pg mL^{-1} KIM-1 + 100.0 pg mL^{-1} BSA, (iv) 5.00 pg mL^{-1} KIM-1 + 100.0 pg mL^{-1} CysC; (v) 5.00 pg mL^{-1} KIM-1 + 100.0 pg mL^{-1} PSA; (B) Stability test of electrochemical KIM-1 immunosensor including 5.00 pg mL^{-1} KIM-1 (n = 6) at 25.0 °C.

standard addition method was applied to the plasma samples, and $y = 1.8993x + 11.1736$, with $R^2 = 0.9993$ was obtained as calibration equation. Thus, the close slope values between direct calibration (inset of Fig. 5) and standard addition methods again verified the high selective acute kidney injury detection.

3.8. Selectivity, stability and reproducibility

For selectivity measurement, the several electrochemical KIM-1 immunosensors were prepared by using different target dispersions such as (i) 100.00 pg mL^{-1} AFP + 100.00 pg mL^{-1} BSA + 100.00 pg mL^{-1} CysC + 100.00 pg mL^{-1} PSA, (ii) 5.00 pg mL^{-1} KIM-1 + 100.0 pg mL^{-1} AFP, (iii) 5.00 pg mL^{-1} KIM-1 + 100.0 pg mL^{-1} BSA, (iv) 5.00 pg mL^{-1} KIM-1 + 100.0 pg mL^{-1} CysC; (v) 5.00 pg mL^{-1} KIM-1 + 100.0 pg mL^{-1} PSA. Afterward, these electrochemical immunosensors were applied to 1.0 mM H$_2$O$_2$ solution. Fig. 6A confirmed that the prepared electrochemical immunosensor demonstrated the high selectivity towards KIM-1.

Fig. 6B demonstrated the stability test results of the prepared electrochemical KIM-1 immunosensor at 25.0 °C for 7 weeks. The immunosensor signals were found about 97.81% of the first electrochemical signal, implying the high stability of immunosensor.

Finally, for reproducibility, 15 different electrochemical KIM-1 immunosensors were developed by the same protocol which was explained in section of 2.8. The relative standard deviation (RSD) was calculated as 0.49 by using the recorded electrochemical signals of 15 different KIM-1 immunosensors, confirming the high reliability of immunosensor production procedure.

4. Conclusions

In this work, sensitive and selective electrochemical kidney injury molecule-1 immunosensor based on covalent organic frameworks-gold nanoparticles (COFs-AuNPs) composite as electrochemical sensor platform and porous NiCo$_2$S$_4$@CeO$_2$ microspheres as signal amplification was reported. The proposed immunosensor was constructed by capture antibody immobilization via gold-amino affinity and secondary antibody incubation via strong electrostatic interaction. Hence, the stable electrochemical signals were accomplished in terms of acute kidney injury disease detection. In addition, the prepared electrochemical immunosensor offered excellent ability in selective and sensitive determination of kidney injury molecule-1 in a short response time. Moreover, it was confirmed that the prepared immunosensor was reproducible biosensor and did not include in time-consuming steps such as sensor preparation.

CRediT authorship contribution statement

Havva Boyacıoğlu: Conceptualization, Methodology, Writing – review & editing. **Bahar Bankoğlu Yola:** Data curation, Visualization, Investigation. **Ceren Karaman:** Conceptualization, Methodology, Writing – review & editing. **Onur Karaman:** Formal analysis, Data curation. **Necip Atar:** Writing – original draft, Visualization, Investigation. **Mehmet Lütfi Yola:** Supervision, Conceptualization, Writing – review & editing.

Declaration of Competing Interest

The authors declare that they have no known competing financial interests or personal relationships that could have appeared to influence the work reported in this paper.

Acknowledgement

Appendix A. Supplementary material

Supplementary data to this article can be found online at https://doi.org/10.1016/j.apsusc.2021.152093.

References

[1] G.M. Chertow, E. Burdick, M. Honour, J.V. Bonventre, D.W. Bates, Acute kidney injury, mortality, length of stay, and costs in hospitalized patients, J. Am. Soc. Nephrol. 16 (11) (2005) 3365–3370, https://doi.org/10.1681/ASN.2004090740.

[2] A. Levin, D.G. Warnock, R.L. Mehta, J.A. Kellum, S.V. Shah, B.A. Molitoris, C. Ronco, Improving outcomes from acute kidney injury: report of an initiative, Am. J. Kidney Dis. 50 (1) (2007) 1–4, https://doi.org/10.1007/s00467-007-0565-4.

[3] B.A. Molitoris, A. Levin, D.G. Warnock, M. Joannidis, R.L. Mehta, J.A. Kellum, C. Ronco, S.V. Shah, A.K.I.N. Work, Improving outcomes of acute kidney injury: report of an initiative, Nat Clin Pract Nephr 3 (2007) 439–442, https://doi.org/10.1007/s00467-007-0565-4.

[4] C. Guerin, R. Girard, J.M. Selli, J.P. Perdrix, L. Ayzac, Initial versus delayed acute renal failure in the intensive care unit. A multicenter prospective epidemiological study. Rhone-Alpes Area Study Group on Acute Renal Failure, Am. J. Respir. Crit. Care Med. 161 (2000) 872–879, https://doi.org/10.1164/ajrccm.161.3.9809066.

[5] K.R. Tuttle, N.K. Worrall, L.R. Dahlstrom, R. Nandagopal, A.T. Kausz, C.L. Davis, Predictors of ARF after cardiac surgical procedures, Am. J. Kidney Dis. 41 (2003) 76–83, https://doi.org/10.1053/ajkd.2003.50025.

[6] K. Bendjelid, B. Levy, A. Broccard, Intensive care medicine science: an art based on applied physiology? Biomed Res. Int. 2015 (2015) 479134, https://doi.org/10.1155/2015/479134.

[7] P. Kannan, H.Y. Tiong, D.H. Kim, Highly sensitive electrochemical determination of neutrophil gelatinase-associated lipocalin for acute kidney injury, Biosens. Bioelectron. 31 (2012) 32–36, https://doi.org/10.1016/j.bios.2011.09.036.

[8] E.V. Schrezenmeier, J. Barasch, K. Budde, T. Westhoff, K.M. Schmidt-Ott, Biomarkers in acute kidney injury - pathophysiological basis and clinical performance, Acta Physiol. (Oxf.) 219 (2017) 554–572, https://doi.org/10.1111/apha.12764.

[9] S.S. Waikar, R.A. Betensky, J.V. Bonventre, Creatinine as the gold standard for kidney injury biomarker studies? Nephrol. Dial. Transpl. 24 (2009) 3263–3265, https://doi.org/10.1093/ndt/gfp428.

[10] J.A. George, V. Gounden, Novel glomerular filtration markers, Adv. Clin. Chem. 88 (2019) 91–119, https://doi.org/10.1016/bs.acc.2018.10.005.

[11] Y. Zhang, W. Zhang, Q. Zhang, K.Y. Li, W. Liu, Y. Liu, C.E. Banks, Green electrochemical sensing platforms: utilizing hydroxyapatite derived from natural fish scales as a novel electrochemical material for the sensitive detection of kidney injury molecule 1 (KIM-1), Analyst 139 (2014) 5362–5366, https://doi.org/10.1039/C4AN00957F.

[12] V. Pennemans, L.M. De Winter, E. Munters, T.S. Nawrot, E. Van Kerkhove, J. M. Rigo, C. Reynders, H. Dewitte, R. Carleer, J. Penders, Q. Swennen, The association between urinary kidney injury molecule 1 and urinary cadmium in elderly during long-term, low-dose cadmium exposure: a pilot study, Environ Health-Glob 10 (2011) 77, https://doi.org/10.1186/1476-069X-10-77.

[13] B. Dedeoglu, H.R.H. de Geus, G. Fortrie, M.G.H. Betjes, Novel biomarkers for the prediction of acute kidney injury in patients undergoing liver transplantation, Biomark. Med. 7 (6) (2013) 947–957, https://doi.org/10.2217/bmm.13.91.

[14] C.F. Zhang, H.J. Wang, Z.H. Tong, C. Wang, Y.S. Wang, H.Q. Yang, R.Y. Gao, H. Z. Shi, The diagnostic and prognostic values of serum and urinary kidney injury molecule-1 and neutrophil gelatinase-associated lipocalin in sepsis induced acute renal injury patients, Eur. Rev. Med. Pharmaco. 24 (2020) 5604–5617, https://doi.org/10.26355/eurrev_202005_21346.

[15] X. Shao, L. Tian, W. Xu, Z. Zhang, C. Wang, C. Qi, Z. Ni, S. Mou, H. Bruns, Diagnostic Value of Urinary Kidney Injury Molecule 1 for Acute Kidney Injury: A Meta-Analysis, PLoS ONE 9 (1) (2014) e84131, https://doi.org/10.1371/journal.pone.0084131.

[16] X. Sun, L. Zhang, X. Zhang, X. Liu, J. Jian, D. Kong, D. Zeng, H. Yuan, S. Feng, Electrochemical dopamine sensor based on superionic conducting potassium ferrite, Biosens. Bioelectron. 153 (2020) 112045, https://doi.org/10.1016/j.bios.2020.112045.

[17] P. Samadi Pakchin, M. Fathi, H. Ghanbari, R. Saber, Y. Omidi, A novel electrochemical immunosensor for ultrasensitive detection of CA125 in ovarian cancer, Biosens. Bioelectron. 153 (2020) 112029, https://doi.org/10.1016/j.bios.2020.112029.

[18] N. Özcan, C. Karaman, N. Atar, O. Karaman, M.L. Yola, A novel molecularly imprinting biosensor including graphene quantum dots/multi-walled carbon nanotubes composite for interleukin-6 detection and electrochemical biosensor validation, Ecs J. Solid State Sc. 9 (12) (2020) 121010, https://doi.org/10.1149/2162-8777/abd149.

[19] X. Wang, W. Cao, L. Qin, T. Lin, W. Chen, S. Lin, J. Yao, X. Zhao, M. Zhou, C. Hang, H. Wei, Boosting the peroxidase-like activity of nanostructured nickel by inducing its 3+oxidation state in LaNiO3 perovskite and its application for biomedical assays, Theranostics 7 (8) (2017) 2277–2286, https://doi.org/10.7150/thno.19257.

[20] J. Tang, D. Tang, Non-enzymatic electrochemical immunoassay using noble metal nanoparticles: a review, Microchim. Acta 182 (13–14) (2015) 2077–2089, https://doi.org/10.1007/s00604-015-1567-6.

[21] C. Karaman, O. Karaman, N. Atar, M.L. Yola, Electrochemical immunosensor development based on core-shell high-crystalline graphitic carbon nitride@carbon dots and Cd0.5Zn0.5S/d-Ti3C2Tx MXene composite for heart-type fatty acid-binding protein detection, Microchim. Acta 188 (2021) 1–15, https://doi.org/10.1007/s00604-021-04838-6.

[22] H. Medetalibeyoglu, M. Beytur, O. Akyildirim, N. Atar, M.L. Yola, Validated electrochemical immunosensor for ultra -sensitive procalcitonin detection: carbon electrode modified with gold nanoparticles functionalized sulfur doped MXene as sensor platform and carboxylated graphitic carbon nitride as signal amplification, Sensor Actuat. B-Chem. 319 (2020) 128195, https://doi.org/10.1016/j.snb.2020.128195.

[23] B. Rezaei, A.M. Shoushtari, M. Rabiee, L. Uzun, W.C. Mak, A.P.F. Turner, An electrochemical immunosensor for cardiac Troponin I using electrospun carboxylated multi-walled carbon nanotube-whiskered nanofibres, Talanta 182 (2018) 178–186, https://doi.org/10.1016/j.talanta.2018.01.046.

[24] M.L. Yola, N. Atar, Amperometric galectin-3 immunosensor-based gold nanoparticle-functionalized graphitic carbon nitride nanosheets and core-shell Ti-MOF@COFs composites, Nanoscale 12 (2020) 19824–19832, https://doi.org/10.1039/D0NR05614F.

[25] A. Simic, D. Manojlovic, D. Segan, M. Todorovic, Electrochemical Behavior and antioxidant and prooxidant activity of natural phenolics, Molecules 12 (2007) 2327–2340, https://doi.org/10.3390/12102327.

[26] J.C. Yi, P.A. Wu, G.Y. Li, W. Xiao, L. Li, Y.Y. He, Y.F. He, P. Ding, C.M. Chen, A composite prepared from carboxymethyl chitosan and aptamer-modified gold nanoparticles for the colorimetric determination of Salmonella typhimurium, Microchim. Acta 186 (2019) 711, https://doi.org/10.1007/s00604-019-3827-5.

[27] R. Ahmad, N. Griffete, A. Lamouri, N. Felidj, M.M. Chehimi, C. Mangeney, Nanocomposites of gold nanoparticles@molecularly imprinted polymers: chemistry, processing, and applications in sensors, Chem. Mater. 27 (2015) 5464–5478, https://doi.org/10.1021/acs.chemmater.5b00138.

[28] B.P. Biswal, H.D. Chaudhari, R. Banerjee, U.K. Kharul, Chemically stable covalent organic framework (COF)-polybenzimidazole hybrid membranes: enhanced gas separation through pore modulation, Chem-Eur J 22 (2016) 4695–4699, https://doi.org/10.1002/chem.201504836.

[29] Y.L. Li, J.Q. Zhang, K.M. Zuo, Z.P. Li, Y. Wang, H. Hu, C.Y. Zeng, H.J. Xu, B. S. Wang, Y.A. Gao, Covalent organic frameworks for simultaneous CO2 capture and selective catalytic transformation, Catalysts 11 (2021) 1133, https://doi.org/10.3390/catal11091133.

[30] Y.F. Zeng, R.Q. Zou, Y.L. Zhao, Covalent organic frameworks for CO2 capture, Adv. Mater. 28 (2016) 2855–2873, https://doi.org/10.1002/adma.201505004.

[31] S. Lin, C.S. Diercks, Y.-B. Zhang, N. Kornienko, E.M. Nichols, Y. Zhao, A.R. Paris, D. Kim, P. Yang, O.M. Yaghi, C.J. Chang, Covalent organic frameworks comprising cobalt porphyrins for catalytic CO2 reduction in water, Science 349 (6253) (2015) 1208–1213, https://doi.org/10.1126/science.aac8343.

[32] A.F.M. EL-Mahdy, C.-H. Kuo, A. Alshehri, C. Young, Y. Yamauchi, J. Kim, S.-W. Kuo, Strategic design of triphenylamine- and triphenyltriazine-based two-dimensional covalent organic frameworks for CO2 uptake and energy storage, J. Mater. Chem. A 6 (40) (2018) 19532–19541, https://doi.org/10.1039/C8TA04781B.

[33] X. Zhang, K.-N. Chi, D.-L. Li, Y. Deng, Y.-C. Ma, Q.-Q. Xu, R. Hu, Y.-H. Yang, 2D-porphrinic covalent organic framework-based aptasensor with enhanced photoelectrochemical response for the detection of C-reactive protein, Biosens. Bioelectron. 129 (2019) 64–71, https://doi.org/10.1016/j.bios.2019.01.009.

[34] R. Zhai, X.Y. Gong, J. Xie, Y.F. Yuan, F. Xu, Y. Jiang, Z.J. Huang, X.H. Dai, Y. J. Zhang, X.H. Qian, X. Fang, Ultrasensitive analysis of heat shock protein 90 alpha with antibodies orderly arrayed on a novel type of immunoprobe based on magnetic COFs, Talanta 191 (2019) 553–560, https://doi.org/10.1016/j.talanta.2018.09.010.

[35] D.B. Shinde, H.B. Aiyappa, M. Bhadra, B.P. Biswal, P. Wadge, S. Kandambeth, B. Garai, T. Kundu, S. Kurungot, R. Banerjee, A mechanochemically synthesized covalent organic framework as a proton-conducting solid electrolyte, J. Mater. Chem. A 4 (7) (2016) 2682–2690, https://doi.org/10.1039/C5TA10521H.

[36] T.-F. Yi, J.-J. Pan, T.-T. Wei, Y. Li, G. Cao, NiCo2S4-based nanocomposites for energy storage in supercapacitors and batteries, Nano Today 33 (2020) 100894, https://doi.org/10.1016/j.nantod.2020.100894.

[37] Z. Wu, X. Pu, X. Ji, Y. Zhu, M. Jing, Q. Chen, F. Jiao, High energy density asymmetric supercapacitors from mesoporous NiCo2S4 nanosheets, Electrochim. Acta 174 (2015) 238–245, https://doi.org/10.1016/j.electacta.2015.06.011.

[38] S. Shi, Z. Sun, Y.H. Hu, Synthesis, stabilization and applications of 2-dimensional 1T metallic MoS2, J. Mater. Chem. A 6 (47) (2018) 23932–23977, https://doi.org/10.1039/C8TA08152B.

[39] P. Guo, H. Song, Y. Liu, C. Wang, CuFeS2 quantum dots anchored in carbon frame: superior lithium storage performance and the study of electrochemical mechanism, Acs Appl. Mater. Int. 9 (37) (2017) 31752–31762, https://doi.org/10.1021/acsami.7b06685.

[40] Y. Luan, H. Zhang, F. Yang, J. Yan, K. Zhu, K. Ye, G. Wang, K. Cheng, D. Cao, Rational design of NiCo2S4 nanoparticles @ N-doped CNT for hybrid supercapacitor, Appl. Surf. Sci. 447 (2018) 165–172, https://doi.org/10.1016/j.apsusc.2018.03.236.

[41] L. Niu, Y. Wang, F. Ruan, C. Shen, S. Shan, M. Xu, Z. Sun, C. Li, X. Liu, Y. Gong, In situ growth of NiCo2S4@Ni3V2O8 on Ni foam as a binder-free electrode for asymmetric supercapacitors, J. Mater. Chem. A 4 (15) (2016) 5669–5677, https://doi.org/10.1039/C6TA00078A.

[42] H. Xing, G. Long, J. Zheng, H. Zhao, Y. Zong, X. Li, Y. Wang, X. Zhu, M. Zhang, X. Zheng, Interface engineering boosts electrochemical performance by fabricating CeO2@CoP Schottky conjunction for hybrid supercapacitors, Electrochim. Acta 337 (2020) 135817, https://doi.org/10.1016/j.electacta.2020.135817.

[43] J. Su, H. Song, C. Wang, Morphology reshaping enabling self-densification of manganese oxide hybrid materials for high-density lithium storage anodes, Adv. Funct. Mater. 29 (51) (2019) 1907154, https://doi.org/10.1002/adfm.v29.5110.1002/adfm.201907154.

[44] S. Lu, S. Wang, P. Wu, D. Wang, J. Yi, L. Li, P. Ding, H. Pan, A composite prepared from covalent organic framework and gold nanoparticles for the electrochemical determination of enrofloxacin, Adv. Powder Technol. 32 (6) (2021) 2106–2115, https://doi.org/10.1016/j.apt.2021.04.025.

[45] M.Lütfi. Yola, N. Atar, M.S. Qureshi, Z. Üstündağ, A.O. Solak, Electrochemically grafted etodolac film on glassy carbon for Pb(II) determination, Sensor Actuat. B-Chem. 171-172 (2012) 1207–1215, https://doi.org/10.1016/j.snb.2012.06.082.

[46] Y.R. Zhu, X.Z. Li, X.Q. Lai, Y. Xie, Y.M. Li, T.F. Yi, Construction of porous NiCo2S4@CeO2 microspheres composites for high-performance pseudocapacitor electrode by morphology reshaping, Mater. Today Chem. 20 (2021) 100448, https://doi.org/10.1016/J.MTCHEM.2021.100448.

[47] M.L. Yola, N. Atar, Development of cardiac troponin-I biosensor based on boron nitride quantum dots including molecularly imprinted polymer, Biosens. Bioelectron. 126 (2019) 418–424, https://doi.org/10.1016/j.bios.2018.11.016.

[48] A. Singh, S.K. Ojha, M. Singh, A.K. Ojha, Controlled synthesis of NiCo2S4@NiCo2O4 core@Shell nanostructured arrays decorated over the rGO sheets for high-performance asymmetric supercapacitor, Electrochim. Acta 349 (2020) 136349, https://doi.org/10.1016/j.electacta.2020.136349.

[49] W.L. Li, Z.X. Song, X.H. Deng, X.Z. Fu, J.L. Luo, Decoration of NiO hollow spheres composed of stacked nanosheets with CeO2 nanoparticles: Enhancement effect of CeO(2)for electrocatalytic methanol oxidation, Electrochim. Acta 337 (2020) 135684, https://doi.org/10.1016/j.electacta.2020.135684.

[50] V.H. Nguyen, J.J. Shim, In situ growth of hierarchical mesoporous NiCo2S4@MnO2 arrays on nickel foam for high-performance supercapacitors, Electrochim. Acta 166 (2015) 302–309, https://doi.org/10.1016/j.electacta.2015.03.069.

[51] X.P. Han, W. Zhang, X.Y. Ma, C. Zhong, N.Q. Zhao, W.B. Hu, Y.D. Deng, Identifying the activation of bimetallic sites in NiCo2S4@g-C3N4-CNT hybrid electrocatalysts for synergistic oxygen reduction and evolution, Adv. Mater. 31 (2019) 1808281, https://doi.org/10.1002/adma.201808281.

[52] J.G. Wang, D.D. Jin, R. Zhou, C. Shen, K.Y. Xie, B.Q. Wei, One-step synthesis of NiCo2S4 ultrathin nanosheets on conductive substrates as advanced electrodes for high-efficient energy storage, J. Power Sources 306 (2016) 100–106, https://doi.org/10.1016/j.jpowsour.2015.12.014.

[53] L.H. Cui, J.W. Cui, H.M. Zheng, Y. Wang, Y.Q. Qin, X. Shu, J.Q. Liu, Y. Zhang, Y. C. Wu, Construction of NiO/MnO2/CeO2 hybrid nanoflake arrays as platform for electrochemical energy storage, J. Power Sources 361 (2017) 310–317, https://doi.org/10.1016/j.jpowsour.2017.07.013.

[54] X.H. Su, L. Yu, G. Cheng, H.H. Zhang, M. Sun, L. Zhang, J.J. Zhang, Controllable hydrothermal synthesis of Cu-doped delta-MnO2 films with different morphologies for energy storage and conversion using supercapacitors, Appl. Energ. 134 (2014) 439–445, https://doi.org/10.1016/j.apenergy.2014.08.050.

[55] C. Karaman, O. Karaman, N. Atar, M.L. Yola, Tailoring of cobalt phosphide anchored nitrogen and sulfur co-doped three dimensional graphene hybrid: boosted electrocatalytic performance towards hydrogen evolution reaction, Electrochim. Acta 380 (2021) 138262, https://doi.org/10.1016/j.electacta.2021.138262.

[56] C. Karaman, O. Karaman, N. Atar, M.L. Yola, Sustainable electrode material for high-energy supercapacitor: biomass-derived graphene-like porous carbon with three-dimensional hierarchically ordered ion highways, PCCP 23 (2021) 12807–12821, https://doi.org/10.1039/D1CP01726H.

[57] L. Chen, Y.T. He, Z.X. Lei, C.L. Gao, Q. Xie, P. Tong, Z. Lin, Preparation of core-shell structured magnetic covalent organic framework nanocomposites for magnetic solid-phase extraction of bisphenols from human serum sample, Talanta 181 (2018) 296–304, https://doi.org/10.1016/j.talanta.2018.01.036.

[58] T. Zhang, Y.L. Chen, W. Huang, Y. Wang, X.Y. Hu, A novel AuNPs-doped COFs composite as electrochemical probe for chlorogenic acid detection with enhanced sensitivity and stability, Sensor Actuat. B-Chem. 276 (2018) 362–369, https://doi.org/10.1016/j.snb.2018.08.132.

[59] J.L. Segura, M.J. Mancheno, F. Zamora, Covalent organic frameworks based on Schiff-base chemistry: synthesis, properties and potential applications, Chem. Soc. Rev. 45 (2016) 5635–5671, https://doi.org/10.1039/C5CS00878F.

[60] C.J. Liu, W. Yang, X. Min, D.C. Zhang, X.H. Fu, S.J. Ding, W.C. Xu, An enzyme-free electrochemical immunosensor based on quaternary metallic/nonmetallic PdPtBP alloy mesoporous nanoparticles/MXene and conductive CuCl2 nanowires for ultrasensitive assay of kidney injury molecule-1, Sensor Actuat. B-Chem. 334 (2021) 129585, https://doi.org/10.1016/j.snb.2021.129585.

[61] Z.M.A.N.H. Lah, S.A.A. Ahmad, M.S. Zaini, M.A. Kamarudin, An electrochemical sandwich immunosensor for the detection of HER2 using antibody-conjugated PbS quantum dot as a label, J. Pharmaceut. Biomed. 174 (2019) 608–617, https://doi.org/10.1016/j.jpba.2019.06.024.

[62] J.C. Zuaznabar-Gardona, A. Fragoso, Development of highly sensitive IgA immunosensors based on co-electropolymerized L-DOPA/dopamine carbon nano-onion modified electrodes, Biosens. Bioelectron. 141 (2019) 111357, https://doi.org/10.1016/j.bios.2019.111357.

[63] T.Z. Liu, R. Hu, Y. Liu, K.L. Zhang, R.Y. Bai, Y.H. Yang, Amperometric immunosensor based on covalent organic frameworks and Pt/Ru/C nanoparticles for the quantification of C-reactive protein, Microchim. Acta 187 (2020) 320, https://doi.org/10.1007/s00604-020-04286-8.